Thermoacoustic Instabilities in Gas Turbines and Rocket Engines: Industry meets Academia
May 30 – June 02, 2016
Munich, Germany
Paper No.: GTRE-009

G-equation modelling of thermo-acoustic oscillations of partially-premixed flames

Bernhard Semlitsch[1], Alessandro Orchini[1], Ann P. Dowling[1] and Matthew P. Juniper[1]

Abstract

Self-excited oscillations of unsteady heat release and acoustic waves cannot be entirely avoided for all operating conditions of gas turbines equipped with lean-burn technology. Nevertheless, safe operability can be guaranteed as long as thermo-acoustic limit cycles are diminished to tolerable amplitudes. Numerical simulations aid combustor design to avoid and reduce thermo-acoustic oscillations. Non-linear heat release rate estimation and its modelling are essential for the prediction of saturation amplitudes of limit cycles. The heat release dynamics of arbitrarily-complex flames can be approximated by a Flame Describing Function (FDF). To calculate an FDF, a wide range of forcing amplitudes and frequencies needs to be considered. For this reason, we present a computationally inexpensive level-set approach, which accounts for equivalence ratio perturbations while modelling the velocity fluctuations analytically. The influence of flame parameters and modelling approaches on flame describing functions and time delay coefficient distributions are discussed in detail. The numerically-obtained flame describing functions are compared with experimental data and used in an acoustic network model for limit cycle prediction. A reasonable agreement of the heat release gain and limit cycle frequency is achieved. However, the phase decay is over-predicted, which can be attributed to the fact that turbulence is neglected. The lack of turbulent dispersion causes a highly correlated heat release response, which is artificial.

Keywords

Thermo-acoustic instability, Non-linear combustion modelling, Flame describing function, G-equation, Equivalence ratio

Introduction

A gas turbine combustor can behave as a self-sustained acoustic resonator. Acoustic waves generated by unsteady combustion are reflected back towards their origin, provoking unsteady heat release. If high heat release occurs sufficiently in phase with high pressure then periodic or quasi-periodic oscillations can be self-sustained. These oscillations can lead to undesirable consequences, such as flame blow off, flashback, or even fatigue of the combustor. Lean-burn flames are particularly receptive to such thermo-acoustic oscillations. Nevertheless, lean burn flames are increasingly popular in combustion applications because they have low $\mathrm{NO_x}$ emissions, which helps to comply with increasingly stringent legislation.

Ideally, potentially damaging thermo-acoustic oscillations will be identified at an early stage in the design process. In order to be practical, this requires numerically-efficient techniques so that a wide range of designs can be screened.

In gas turbines, thermo-acoustic oscillations usually cannot be avoided for all operating conditions. However, safe operability can be assured as long as self-excited oscillations are restricted to tolerable amplitudes. In such scenarios, flame describing functions $\mathcal{F}(F_A, f)$, being dependent on forcing amplitudes F_A and frequencies f, can be used to characterise the non-linear flame response (in terms of heat release rate $\dot{q}$) when forced with a harmonic perturbation,

$$\frac{\dot{q}'}{\bar{\dot{q}}} = \mathcal{F}(F_A, f)\frac{u'_B}{\overline{u_B}} = g \cdot e^{i\varphi}\frac{u'_B}{\overline{u_B}}\,, \qquad (1)$$

where g is the gain, φ is the phase delay, and u_B is the imposed velocity disturbance just upstream of the burner orifice. Overbars and primes denote mean averaged and Fourier transformed quantities, respectively. The FDF can be determined using experimental measurements or numerical simulations and expressed as the sum of time delays, $\Delta\tau$, with coefficients k_n:

$$\mathcal{F}(F_A, f) = \frac{\dot{q}'/\bar{\dot{q}}}{u'_B/\overline{u_B}} \approx \sum_{n=1}^{N} k_n(F_A)e^{-i2\pi f n\Delta\tau}\,. \qquad (2)$$

These parameters, k_n and $\Delta\tau$, relate the amplification of the heat release response to a disturbance generated by acoustic waves at the fuel injection location or flame base and being retarded by the disturbance convection time. The time delay constants can be found by $k_n(F_A) = g(n\Delta\tau, F_A)\Delta\tau$, where $g(t, F_A)$ is the impulse response of the flame, which is calculated by applying the one-sided inverse Fourier transform on the flame describing function. In order to reconstruct the flame describing function by the sum of time delays, the calculated time delay constants are substituted

[1]University of Cambridge, Department of Engineering, UK

Corresponding author:
Bernhard Semlitsch, University of Cambridge, Department of Engineering, Trumpington Street, Cambridge, Cambridgeshire, CB2 1PZ, UK.
Email: bs564@cam.ac.uk

into Eq. 2,

$$\mathcal{F}(F_A, f) = \int_0^\infty g(t, F_A) e^{-i\omega t} dt \approx \sum_{n=1}^{N} g(n\Delta\tau, F_A) e^{-i\omega n\Delta\tau} \Delta\tau \,. \quad (3)$$

The number of time delays, N, determines the resolution of the FDF over a given frequency range. The predicted limit cycle amplitude become more accurate as N increases. This is particularly evident for the complex flame shapes found in industrial applications (see e.g. Macquisten et al. 2014). Highly accurate but numerically expensive methods restrict the assessment to a few forcing amplitudes and frequencies, which might lead to an inappropriate overall description of the flame dynamics. Therefore inexpensive numerical methods that can provide sufficiently accurate results to predict flame describing function at many forcing amplitudes and frequencies are desired.

The impulse response or sum of time delay coefficients reveal the time scales of the processes leading to a heat release modulation. Huber and Polifke (2009a,b), Komarek and Polifke (2010) and Blumenthal et al. (2013) were able to distinguish the contributions of different mechanisms influencing the heat release by analysing their contribution to the impulse response. It has been suggested by Huber and Polifke (2009a,b) that gains larger than unity can only be achieved with a combination of positive and negative time delay coefficients. Blumenthal et al. (2013) indicated that a negative contribution, corresponding to a phase shift, can be caused by restoration effects for premixed flames. These findings highlight that physical insight can be gained by analysis of the time delay coefficients.

Dowling (1999) demonstrated that flame describing functions obtained from a kinematic flame model can be used to predict thermo-acoustic instabilities appropriately. Such kinematic flame models based on level-set methods are computationally inexpensive, because only essential features are incorporated. Methods presented by Graham and Dowling (2011) can be used even for relatively complex flame shapes. The drawback of Graham and Dowling's implementation, which was to track two flame surfaces in a Lagrangian sense, is the handling of flame-pinching events and the distinction of burned and unburned regions. Due to these shortcomings, the numerical effort becomes high for strongly wrinkled flames, which limits the investigation range.

Numerical predictions based on kinetic flame response representations rely on parameters and simplifying assumptions. For example, the flow-field is commonly idealised and convective effects in the supply duct are neglected. These assumptions demand quantitative validation with experiments to prove reliability. Lieuwen (2003) highlights that the crucial drawback of reduced-order models is still the lack of quantitative validation with experiments.

The main limitations of level set methods modelling the non-linear heat release generated by flames have been the fragility to flame-pinching events and the lack of validation. In order to overcome these problems, we present a level-set method to estimate flame describing functions, which can robustly handle flame pinching and sophisticated flames, such as an M-shaped flame. The computational efficiency of this approach allows evaluation of the flame response for numerous forcing amplitudes and frequencies. Therefore, the complexity of the heat release response can be integrated and analysed for very many time delays and coefficients in acoustic network simulations. We describe the methodology to obtain the heat release rate from kinematic flame simulations in detail and emphasise the validation of the approach. The obtained results under different modelling assumptions are compared with available experimental data. Consequences of the modelling assumptions are pointed out and the results are examined critically.

Methodology - Flame front tracking

Assuming that chemical reactions between fuel and oxidizer occur instantaneously in a thin sheet, the flame front can be regarded as discontinuity dividing reactants and products. The kinematics and surface alterations of the flame front determine its dynamic heat release response. The thin flame burns normal to its front at the flame speed, which is determined by local chemical reaction rates.

A scalar G field indicating the shortest distance to the flame front can be defined, where an arbitrary fixed value G_0, e.g. zero, can be used to identify the flame front location. Values of G larger or smaller than G_0 represent the unburned mixture or products, respectively. By defining the scalar G-field to be smooth and continuous in the spatial domain, the normal $\mathbf{n}$ pointing into the unburned mixture can be calculated by $-\nabla G/|\nabla G|$. Therefore, the convective motion of the flame front is dictated by the local flame speed s_L and the local flow velocity $\mathbf{u}$ at which the reactants arrive. The material derivative of the level-set describes the flame front movement by the so-called G-equation,

$$\frac{DG}{Dt} = \frac{\partial G}{\partial t} + \left(\mathbf{u} - s_L \frac{\nabla G}{|\nabla G|}\right) \cdot \nabla G = 0 \,. \quad (4)$$

With the integration of the implicit G field, a fully non-linear description of the flame dynamics is obtained.

The flame speed s_L depends on the local equivalence ratio ϕ and curvature effects,

$$s_L = c_0 s_L^0 (1 - \mathcal{L}\,\kappa) = c_0 c_1 \phi^{c_2} e^{c_3(\phi - c_4)^2} (1 - \mathcal{L}\,\kappa) \,, \quad (5)$$

where s_L^0 is the burning speed of a flat flame, $\mathcal{L}$ is the Markstein length, and $\kappa = \nabla \cdot \mathbf{n}$ is the local flame curvature. The fuel in the present investigation is ethylene and the flame speed, s_L^0, as a function of the local equivalence ratio, ϕ, can be modelled by fitted factors c_i for the specific reactant media. An additional constant c_0 is introduced (accordingly to the work by Graham and Dowling (2011)) to alter the location of the numerically predicted flame front to that of the experimentally-observed turbulent flame brush.

Table 1. Coefficients used for Eq. 5 to represent ethylene.

$c_0\ (-)$	$c_1\ (m/s)$	$c_2\ (-)$	$c_3\ (-)$	$c_4\ (-)$
1.51314	1.32176	3.11023	1.72307	0.36196

The unsteady heat release rate of an axisymmetric flame can be calculated by spatial integration along its front

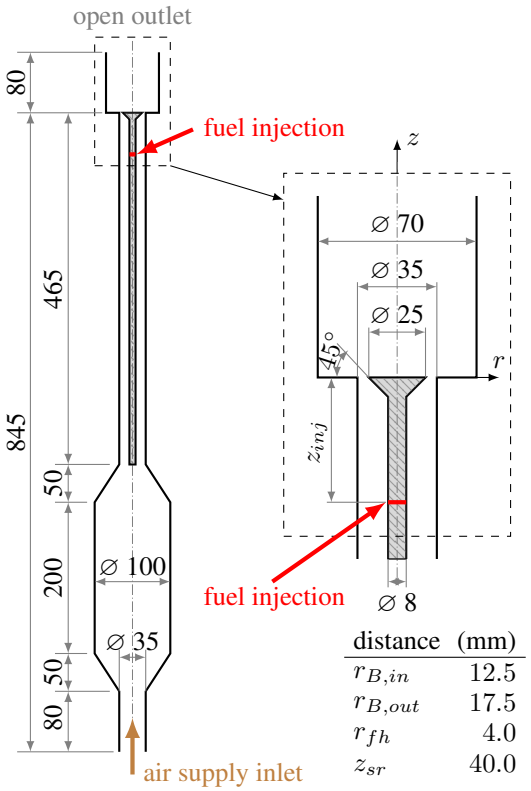

Figure 1. Sketch of the burner developed by Balachandran (2005). All dimensions are in millimetres.

represented by the iso-surface $G = 0$,

$$\dot{q}(t) = 2\pi\rho c_0 s_L^0 \Delta h_R \iint (1 - \mathcal{L}\kappa)|\nabla G|\delta(G) r dr dz \ . \quad (6)$$

The local enthalpy release $\Delta h_R(\phi)$ of the reaction per unit mass is defined as $\Delta h_R = 3.2 \cdot 10^6 (min(1, \phi))/(1 + 0.067\ \phi)\ Jkg^{-1}$. A fast Fourier transform of the heat release rate fluctuations $\dot{q}(t) - \bar{\dot{q}}$ is performed, in which the contribution at the fundamental forcing frequency is extracted to calculate the gain and phase decay as defined in Eq. 1.

Geometry and setup

The geometry of the laboratory combustor illustrated in Fig. 1 is selected for these simulations. It was experimentally investigated by Balachandran (2005). Therefore, comparison of the numerical results with experiments is permitted. The burner consists of a cylindrical pipe with varying cross-section and centred bluff body. At the combustion chamber exit, the flow discharges into quiescent ambient conditions. Self excited thermo-acoustic instabilities were not observed experimentally with a combustion chamber height of 80 mm. Therefore, it was extended to 350 mm to investigate limit cycles.

The fuel is injected through tiny holes around the circumference of the centre body, which are located 55 mm upstream of the burner orifice. The air is supplied far upstream, where the inlet pressure and temperature is assumed to be at ambient conditions in the simulations, i.e. 101325 Pa and 299 K, respectively. The imposed inlet air mass-flow rate ($\dot{m}_{air} = 0.005417\ kg/s$) is estimated such that a velocity of 10 m/s is reached at the burner exit. The employed flame properties are chosen according to the fuel ethylene. The fuel mass flow rate is specified in terms of the equivalence ratio ϕ, which is a parameter in the simulations. The fuel is assumed to mix uniformly with the air at the injection location.

Flow field

Analytical flow and disturbance models meet the requirements for the present purpose and are computationally efficient. The axisymmetric potential flow model developed by Graham and Dowling (2011) is used, in which a spherical point source is placed 40 mm upstream of the burner orifice. This source location z_{sr} determines the directivity of the flow and spread angle of an annular jet exhausting the port. The distance to the spherical source can be expressed as $\xi = \sqrt{r^2 + (z - z_{sr})^2}$. The radial velocity component in the spherical coordinate system can be written in terms of the velocity potential P as $u_\xi = \partial P/\partial\xi$. In order to conserve continuity and to ensure irrotationality, the velocity potential needs to satisfy $\nabla^2 P = 0$. Solutions have the form $P = A_u \xi^n$, where particularly $n = -1$ satisfies these conditions. With $P = A_u/\sqrt{r^2 + (z - z_{sr})^2}$, the velocity components in the cylindrical coordinate system can be written as,

$$u_r = \frac{-A_u\, r}{\sqrt{(r^2 + (z - z_{sr})^2)^3}} \quad (7)$$

and

$$u_z = \frac{-A_u\, (z - z_{sr})}{\sqrt{(r^2 + (z - z_{sr})^2)^3}} \ . \quad (8)$$

The potential amplitude $\overline{A_u}$ can be determined such that a desired mean velocity $\overline{u_B}$ at the burner orifice is obtained,

$$\overline{A_u} = -\overline{u_B} \left(\left(\frac{r_{B,out} + r_{B,in}}{2} \right)^2 + z_{sr}^2 \right) \ , \quad (9)$$

where $r_{B,out}$ and $r_{B,in}$ are the outer and inner radii of the burner orifice, respectively. A velocity perturbation with sinusoidal form can be included into the velocity model by writing,

$$A_u = \overline{A_u} \cdot (1 + F_A \sin(2\pi\ ft)) \ , \quad (10)$$

where F_A is the forcing amplitude and f is the forcing frequency.

Equivalence ratio perturbations The fuel is injected at a location z_{inj} upstream of the burner orifice. Because the mixing process is not considered upstream of the flame, the reactant mixture distribution is passively convected by the mean flow from the injection to the reaction zone. The injected fuel mass flow rate is not significantly influenced by acoustic disturbances and therefore equivalence ratio perturbations can be assumed to be inversely proportional to local air velocity fluctuations at the injector nozzle,

$$\phi'_{inj} = \frac{\overline{\phi}}{\left(1 + F_A \frac{u'_{inj}}{\overline{u_{inj}}}\right)} \ . \quad (11)$$

The equivalence ratio oscillation ϕ'_B passing the burner orifice at time t can be expressed as $\phi'_B(r, z, t) =$

$\phi'_{inj}(r, z, t-\tau)$, where τ represents the retarded time, which is required to convect the disturbance from the injection location to the burner orifice. From this point on, the convection of the equivalence ratio oscillation is simulated.

The mean retarded time can be calculated as $\overline{\tau} = \int_0^z \overline{u}^{-1} dz$, where $\overline{u}$ is the mean velocity in the duct. Figure 1 illustrates the cross-sectional change of the duct due to the flame holder, which results in a flow acceleration. Therefore, the time delays are calculated for the straight annular duct and the section constricted by the bluff body separately. The convection distance past the flame holder is $|z_{fh}| = \left|\frac{r_{B,in}-r_{fh}}{\tan 45°}\right|$, while the convection distance in the straight annular section is $|z_{an}| = |z_{inj} - z_{fh}|$. ($r_{fh}$ is the inner radius of the annular duct.) Since the flow can be assumed to be incompressible in the ducts, the flow velocities are proportional to cross-sectional variations,

$$\overline{u_{an}} = \overline{u_B} \frac{(r_{B,out}^2 - r_{B,in}^2)}{(r_{B,out}^2 - r_{fh}^2)} \tag{12}$$

and

$$\overline{u_{fh}} = \overline{u_B} \frac{(r_{B,out}^2 - r_{B,in}^2)}{(r_{B,out}^2 - z^2 \tan^2(45°))} \,. \tag{13}$$

The retarded times for the two duct sections are,

$$\overline{\tau_{an}} = \frac{r_{B,out}^2 - r_{fh}^2}{\overline{u_B}(r_{B,out}^2 - r_{B,in}^2)} \left(|z_{inj}| - \frac{(r_{B,in} - r_{fh})}{\tan 45°} \right) \tag{14}$$

and

$$\overline{\tau_{fh}} = \frac{r_{B,in} - r_{fh}}{\overline{u_B}(r_{B,out}^2 - r_{B,in}^2)\tan(45°)} \cdot \left(r_{B,out}^2 - \frac{(r_{B,in} - r_{fh})^2}{3} \right) \,. \tag{15}$$

Implementation

The G-field, ϕ-field, boundary conditions, and domain extensions and discretisations are specified in an input file. The extent of the computational domain is outlined in Fig. 2. A regular two-dimensional grid of 441×441 nodes is employed for the numerical discretisation exploiting the axisymmetry of the M-shaped flame, where a grid sensitivity analysis was performed. The numerical mesh starts below the burner orifice in order to facilitate the implementation of the flame boundary conditions at the lip. A strip at the centreline is excluded to reduce the computational effort.

The flow-field can be calculated directly by the analytical expression and is therefore not provided at initialisation. Nevertheless, a uniform equivalence ratio field (set to the mean equivalence ratio $\overline{\phi}$) and a smooth initial G-field satisfying the boundary conditions need to be provided. The steady-state flame evolving without perturbations is used as initial condition for every operating condition.

Executing an iteration, the flow field and velocity oscillations are calculated. The equivalence ratio fluctuations are convected throughout the domain, where a fifth order weighted essentially non-oscillatory WENO scheme is used for spatial discretisation and an implicit third-order Runge-Kutta total variation diminishing scheme is employed for time integration.

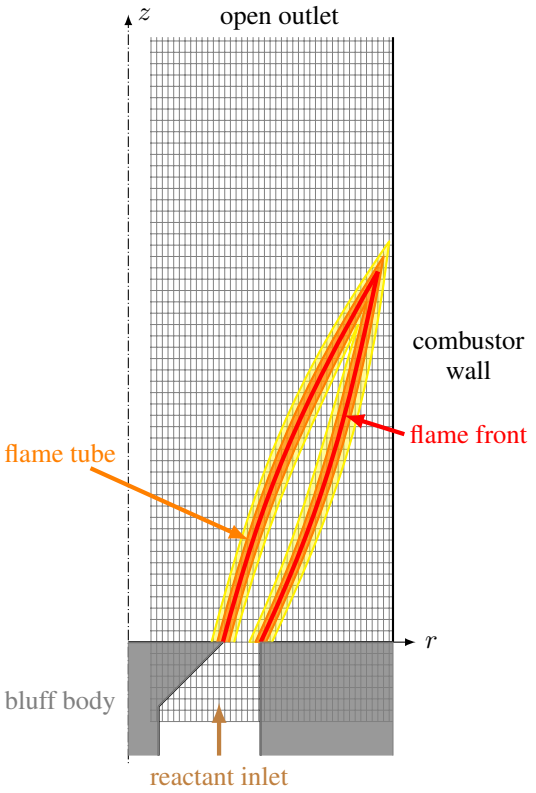

Figure 2. Sketch of the tubes surrounding the flame front, where the orange tube represents $|G| \leq \beta$ and the yellow tube $\beta < |G| \leq \gamma$. (The grid indicates the extent of the two-dimensional axisymmetric computational domain.)

Equation 4 shows that the convection of the G-field is only dependent on the local flow velocity and flame speed. Therefore, only the near-field surrounding the flame front needs to be considered, which is illustrated in Fig. 2 by an orange and a yellow region surrounding the red coloured flame. These represent the two concentric tubes around the zero level-set with constant radii $0 < \beta < \gamma$ from the flame front, which are calculated initially and re-established after each iteration. * The G-field is only convected in the interior of the narrower tube as a signed distance function, whereas constant extremal values are assigned beyond the outer tube. A smooth transition is computed in-between the inner and outer tube. This can be expressed as,

$$\frac{\partial G}{\partial t} + c(G) \left(\mathbf{u} + \mathbf{s_L} \frac{\nabla G}{|\nabla G|} \right) \cdot \nabla G = 0 \,, \tag{16}$$

where

$$c(G) = \begin{cases} 1 & \text{if} \quad |G| \leq \beta \\ (|G| - \gamma)^2 \dfrac{(2|G| + \gamma - 3\beta)}{(\gamma - \beta)^3} & \text{if} \quad \beta < |G| \leq \gamma \\ 0 & \text{if} \quad |G| > \gamma \end{cases} \tag{17}$$

*Enough information around the flame front needs to be considered to compute the spatial gradient of the G-field smoothly. The thickness of the flame tubes have been chosen with reference to the computational cell size, where $\beta = 3$ cells and $\gamma = \beta + 3$ cells.

The spatial and time derivatives are computed with the same discretisation schemes as the equivalence ratio fluctuations, which were mentioned in the preceding paragraph. This so-called narrow band level-set method has been described in more detail by Sethian (2001) and Peng et al. (1999).

Sharp gradients can evolve during the simulation advancement, as e.g. with pinching events. In order to keep the G-field smooth, re-initialisation steps are performed Hartmann et al. (2010), which consists essentially of solving the Eikonal equation $|\nabla G| = 1$. This procedure is performed each time step before a gradient calculation of the updated G-field is required.

The computation of the heat release rate requires the integration at a level-set $G = 0$. Since the flame tubes are used to track the flame front, the flame tubes are rebuilt with the updated information of the G-field after the core processes of the simulation have been performed. A high-order algorithm is used for integration of the flame surface, which is accomplished by using a one step adaptive mesh refinement, subdividing each cell into five node points.

The unsteady heat release and flow velocity are the essential quantities to construct the flame describing function and are therefore saved every time step. The required statistical accuracy governs the simulation duration. Due to the modelling assumptions in the present simulations (absence of sources generating stochastic fluctuations), the heat release rate cycles evolve identically except for negligible errors caused by numerical uncertainty. Therefore, the computation duration can be restricted to the heat release response of the flame on one complete forcing cycle (after the transient). Nonetheless, repeatability has been ensured for the presented data by simulating at least eight full forcing cycles. Only data acquired after the initial transient is considered for the post-processing.

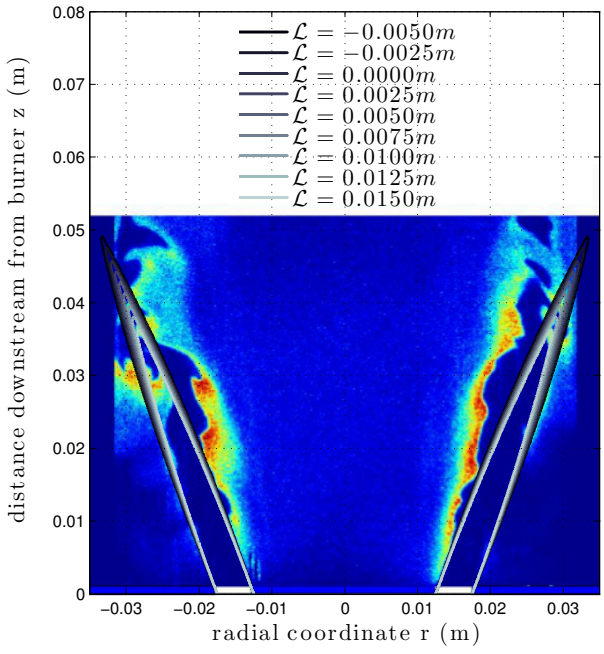

Figure 3. Comparison of the unperturbed flame shape for different Markstein lengths at a mean equivalence ratio $\overline{\phi}$ of 0.55 with an instantaneous OH PLIF image (Balachandran 2005, pp.72).

Validation, comparison to experimental data

The simulation results are compared to previously computed data by Graham and Dowling (2011) and experimental measurements obtained by Balachandran (2005) in order to investigate the validity and uncertainty of the approach.

Firstly, the flame shape relies on many parameters, such as the velocity model, flame speed, and Markstein lengths, and is compared to an experimental image of the flame in Fig. 3. The directivity of the steady flame is estimated consistently and the best agreement in terms of flame length takes place when flame curvature effects are neglected. However, unsteady flow leads to a wrinkled flame shape even without forcing in the experimental setup. These features are not represented in the potential flow model, which accounts only for forced flow disturbances. A perfect comparison with respect to prior simulation data (Graham and Dowling 2011) using a different modelling formulation was achieved.

Flame describing functions have been measured experimentally in the range of 20 to 400 Hz and are compared to the present simulation results in Fig. 4. The prediction of the

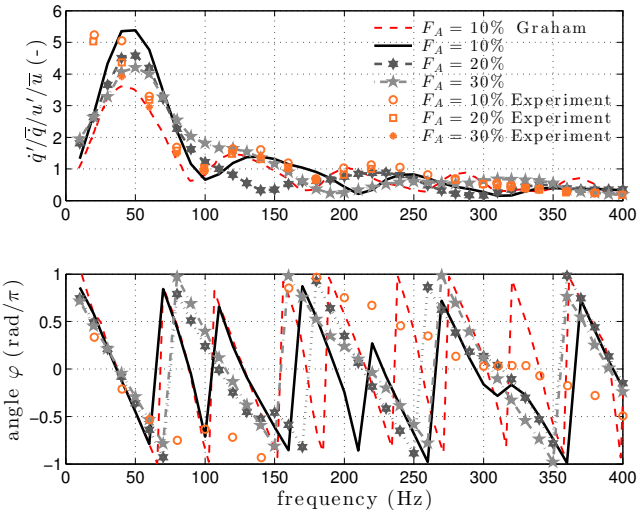

Figure 4. For three forcing aptitudes, the flame describing functions $\mathcal{F}(F_A, \omega)$ obtained with numerical and experimental methods are compared for a mean equivalence ratio $\overline{\phi}$ of 0.55 without considering flame curvature effects.

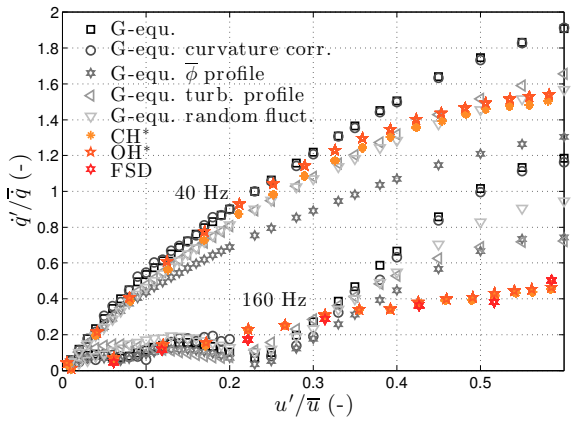

Figure 5. The numerically predicted saturation behaviour of the heat release as function of forcing amplitude is compared with experiments.

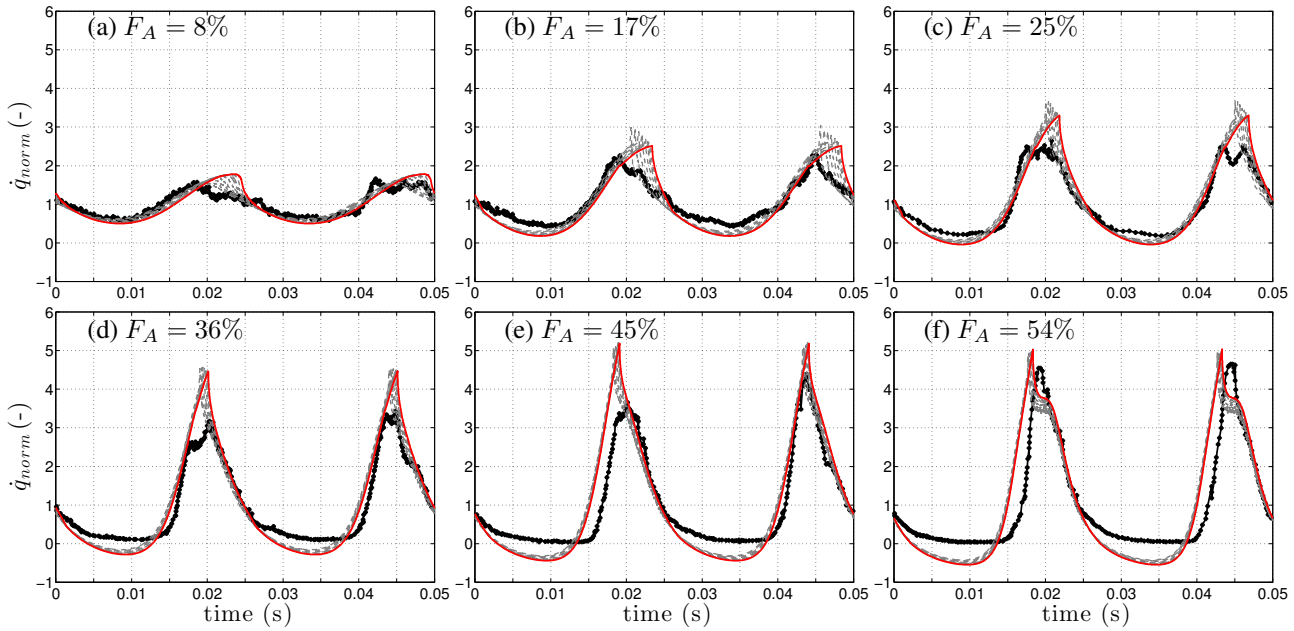

Figure 6. Comparison of the numerically estimated normalised heat release rate $\dot{q}_{norm}$ (red) for different forcing amplitudes with experimentally measured data (black) (see Balachandran 2005, pp.176) for a mean equivalence ratio $\overline{\phi}$ of 0.55 and a forcing frequency of $40\ Hz$. The grey dashed lines indicate the flame curvature effects. (Negative heat release rate values are possible due to the normalisation chosen by Balachandran (2005); $\dot{q}_{norm} = 2 \cdot \dot{q}(t)/\overline{\dot{q}} - 1$.)

gain agrees reasonably with the measurements, considering the simplicity of the velocity model. Nevertheless, the phase decay is very rapid with the present approach at a forcing amplitude of 10% prior to flame pinching. For higher forcing amplitudes, the phase lag decays less steeply, but remains over-predicted compared with the experimentally evaluated behaviour.

Results by Graham and Dowling (2011) are highlighted in Fig. 4 in order to illustrate the differences between Graham and Dowling's linearised G-equation model and the present approach. In particular, the over-prediction of the phase lag is reduced at high frequencies ($> 150\ Hz$).

The saturation behaviour as a function of the forcing amplitude has been measured for two forcing frequencies and is compared to the numerically-predicted saturation amplitudes in Fig. 5. For low forcing frequencies ($< 100\ Hz$), good agreement is achieved at low forcing amplitudes. However, the heat release response is overestimated at high forcing amplitudes. An oscillatory behaviour of the heat release rate as a function of the forcing amplitude arises for higher forcing frequencies ($> 100\ Hz$).

General trends of the instantaneous measured heat release rates (see Balachandran 2005, pp.176) are captured with the numerical approach, as shown in Fig. 6 for different forcing amplitudes at a frequency of $40\ Hz$. The simulations predict, in contrast to the experiments, higher maxima and less heat release inbetween peaks. This discrepancy can be related to the neglected flow recirculation and the temperature distribution used in the computations. The experimental measurements exhibit, in contrast to the simulations, significant cycle-to-cycle variations, which might be induced due to unsteady flow features. Further, dispersive effects translating the locations of the peaks can be observed in the experimentally measured heat release, which may be caused by large-scale turbulence.

Flame describing functions

Firstly, we clarify the individual impact of the simplistic flow and perturbation models on the estimated flame describing function, which is illustrated in Fig. 7. Considering only velocity perturbations (i.e. no equivalence ratio perturbations), Fig. 7(a), the highest gain occurs at zero frequency and decays rapidly with small regular oscillations at approximately every $80\ Hz$. The velocity perturbation amplitudes depend linearly on the forcing amplitude (see Eq. 10) so the gain is constant with amplitude.

Considering only equivalence ratio perturbations (i.e. no velocity perturbations in the combustion chamber), a more elaborate gain pattern can be observed, as shown in Fig. 7 (b). Dominant features are the high magnitude peaks at low forcing frequencies, a linear regime at low forcing amplitudes and a regime exposing different heat release characteristics at high forcing amplitudes when the local equivalence ratio can become close to the stoichiometric ratio. At intermediate forcing amplitudes, an inclined gain interference pattern can be observed.

Combining the effects of velocity and equivalence ratio perturbations causes essentially the same gain pattern as that without velocity perturbations, but with an additional horizontal interference pattern (which is notable especially at high forcing amplitudes). Thus, velocity perturbations affect the gain magnitude indirectly (with the present velocity model) by influencing equivalence ratio perturbations with respect to the flame front rather than generating heat release oscillations directly. The frequency of this interference effect is governed by the phase relation between velocity and equivalence ratio perturbations. Figure 7 (d) shows that shifting the injection location closer to the burner orifice and altering thereby the phase relation decreases the frequency of this horizontal interference pattern.

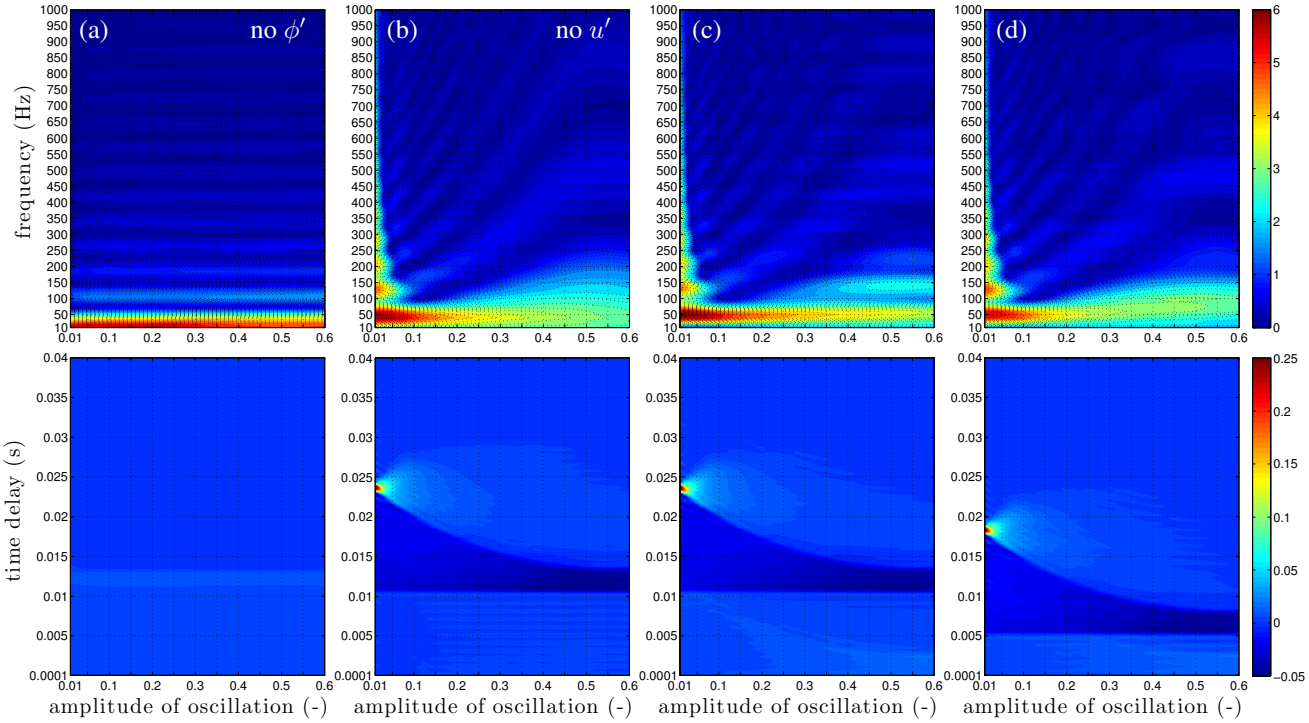

Figure 7. The flame describing function gain and the time delay coefficients for a mean equivalence ratio $\overline{\phi}$ of 0.55 are illustrated for different modelling procedures; (a) only the velocity perturbations (the gain is upscaled by a factor of four for this case), (b) only equivalence ratio perturbations, (c) velocity and equivalence ratio perturbations, and (d) velocity and equivalence ratio perturbations with fuel injection location at $z_{inj} = 27.5\ mm$ (closer to the burner) are considered. The number of time delay coefficients is 800, where $\Delta\tau$ is $0.05\ ms$.

The time delay coefficients (as defined in Eq. 2) enhance physical interpretation of the Flame Describing Function. These show the amplitude of the heat release at a range of times after the reference velocity signal. From the convection time, the heat release location can be inferred, which can also be compared with images of the flame. In figure Fig. 7 (a), the higher values, which occur around $\tau = 0.012$, correspond to the propagation time of the velocity disturbances to the flame tip. In this case, which has no equivalence ratio perturbations, the heat release modulation is generated mostly due to the flame tip motion caused by velocity perturbations. Due to the definition of the flame describing function in Eq. 1, a positive contribution due to velocity perturbations is expected.

For stiff fuel injection systems and quasi-steady forced oscillations, equivalence ratio perturbations and air stream fluctuations are proportional to each other, $\phi'/\overline{\phi} \sim -u'_{inj}/\overline{u_{inj}}$, where the index inj references the velocity u to the injection location. Because the velocity perturbations in the supply duct are caused by acoustic waves, the velocity fluctuations propagate instantly to the burner orifice, i.e. $u'_{inj}/\overline{u_{inj}} \approx u'_B/\overline{u_B}$. Thus, the heat release rate response provoked by velocity and equivalence perturbations are out of phase, which manifests itself as sign change in the time delay coefficients. Therefore, a horizontal border separates positive and negative coefficients at a time delay of approximately $0.01\ s$ in Fig. 7 (b), which represents the intrinsic time delay accounting for the equivalence ratio fluctuation convection from the fuel injection location to the flame base. This intrinsic time delay is altered by a shift of the fuel injection location, as shown in Fig. 7 (d).

The curved border visible in the time delay frames (bottom frames) of Fig. 7(b–d) indicates the propagation time of the equivalence ratio oscillations from the injector to the first flame-pinching event, which can be seen in Fig. 9. This flame pinching leads to the disappearance of the high equivalence ratio perturbations that cause this event. Therefore, only low equivalence ratio perturbations remain on the flame front beyond this propagation time. These are in phase with the velocity perturbations and contribute positively to the coefficients at later time delays.

For very low forcing amplitudes, the heat release rate modulation is concentrated at the flame tip independently of the forcing frequency, because relatively small equivalence ratio perturbations do not lead to flame pinching and are therefore not completely burned before reaching the flame tip. Another way to look at this is that the time delay coefficients of one forcing amplitude represent an integration over all forcing frequencies, which results in a high time delay coefficient associated with the equivalence ratio perturbations modulating the heat release rate at the flame tip.

When equivalence ratio fluctuations are present, it is worth noting that the velocity perturbations also contribute to the time delay coefficients. Elevated positive values are notable in Figs. 7 (c) and (d) (as compared with Fig. 7 (b)) at time delays lower that $0.01\ s$, which mimic the negative shape with the curved border caused by the equivalence ratio perturbations at later time delays. This demonstrates that velocity perturbations affect indirectly the heat release rate when equivalence ratio perturbations are present.

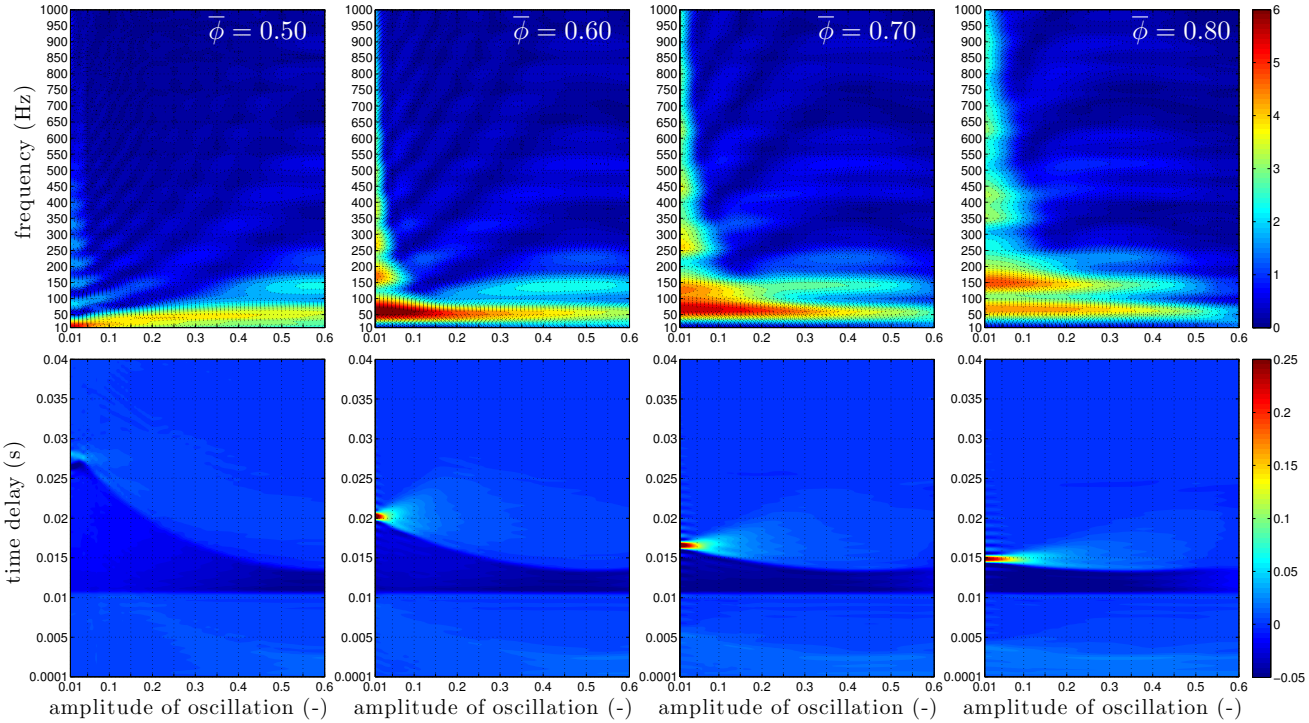

Figure 8. Flame describing function gains and time delay constants for different mean equivalence ratios.

Gain distribution The mean velocity and equivalence ratio define the overall distribution of the heat release rate amplification as functions of forcing amplitude and frequency, which is discussed further in the following paragraphs. The evolution for different equivalence ratios is shown in Fig. 8, where the fuel injection location is unchanged. The horizontal interference pattern caused by the velocity perturbations can be observed for all mean equivalence ratios appearing at the same forcing frequencies.

Dominant high-amplitude peaks appear at low forcing frequencies (50 to 150 Hz), at the half wavelength of the equivalence ratio oscillation corresponding to the flame length. Therefore, maximal oscillations in the unsteady heat release are induced by the alternating appearing equivalence ratio fluctuations. For higher mean equivalence ratios, the flame length becomes shortened and therefore the frequency at which this peak occurs is increased. Further, this dominant peak is widened over a larger forcing frequency range for higher mean equivalence ratios. The horizontal interference pattern caused by the velocity fluctuations splits this dominant gain elevation at low frequencies for higher mean equivalence ratios ($\overline{\phi} > 0.7$).

At low forcing amplitudes, the equivalence ratio perturbations are too small to cause flame pinching and the foremost modulation of heat release is generated by equivalence ratio perturbations at the flame tip. When the wavelength of the equivalence ratio perturbations on the flame front is a multiple of the flame length, a high equivalence ratio perturbation disappears at the flame tip and a high equivalence ratio perturbation arises at the flame base. These effects balance in terms of heat release rate generation, which evolves therefore relatively constant over a forcing cycle. In contrast, when the high equivalence ratio perturbations on the flame front form odd multiples of one half, a maximal modulation of the unsteady heat release is induced. This leads to high gain responses and a regular spaced pattern can be observed in this linear regime at low forcing amplitudes. The importance of individual equivalence ratio maxima is reduced with the number of extrema existing on the flame front and this regime becomes narrower with increasing forcing frequency.

The flame speed is low for mean equivalence ratios below 0.50. Therefore, the flame is impractically elongated and penetrates the combustor walls. Hence, the importance of the heat release modulation at the flame tip diminishes. Equivalence ratio fluctuations generate a higher heat release rate response, when the wavelength matches the geometrical constrains of the burner. At higher forcing amplitudes, the flame speed increases and the flame becomes short enough that the fronts interact before penetration.

Interesting to note is the manifestation of the wall interaction in terms of time delay coefficients, where the high peak value due to flame tip modulation is replaced by a bifurcated value distribution.

An inclined interference pattern generated by equivalence ratio fluctuations and flame pinching can be observed in Fig. 8, which is illustrated quantitatively in Fig. 9 by showing the heat release rate over one forcing cycle at constant forcing amplitude. Abrupt alterations of the unsteady heat release can only be provoked by events in which the flame front disappears suddenly, e.g. flame/wall interactions or pinching effects. Thus, flame pinching is the mechanism generating the cusps visible in Fig. 9. On the other hand, the appearance of equivalence ratio patterns at the flame base and their propagation on the flame front changes the heat release rate continuously.

The inclined interference pattern continues beyond the linear regime, since these patterns are generated by principally the same mechanism. However, flame pinching occurs within the inclined interference pattern region, but

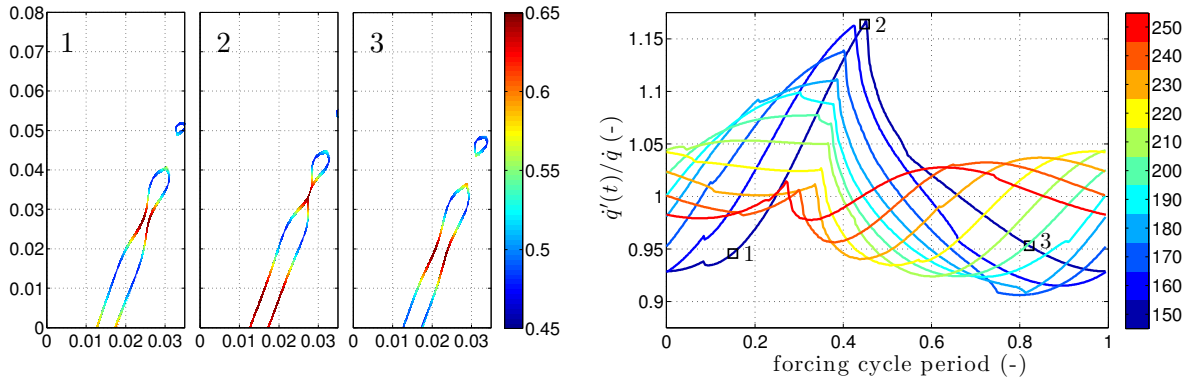

Figure 9. The flame front coloured by the equivalence ratio for a forcing amplitude of $F_A = 15\%$ is illustrated to the left for a mean equivalence ratio $\overline{\phi}$ of 0.55 and a forcing frequency of $150\ Hz$. To the right, the evolution of the heat release rate over one forcing cycle is shown for a frequency range. (The squares with numbers indicate the instants (left) to the overall heat release rate (right).

not in the linear regime. Figure 9 (2) shows that a maximal instantaneous heat release is generated when a maximal number of high equivalence ratio perturbations are burning on the flame front. The flame is pinching and a high equivalence ratio perturbation is convecting on the flame base. By the instant shown in Fig. 9 (3), the high equivalence ratio perturbation causing the pinch-off is burned and a low equivalence ratio perturbation is propagating at the flame base. This situation causes a very low heat release rate. Therefore, a maximal heat release modulation is reached. The inverse effect takes place (see the heat release rate at $240\ Hz$) when a flame pinching occurs while a low equivalence ratio perturbation is propagating at the flame base.

The inclined interference pattern is caused by the interaction of at least two equivalence ratio perturbation maxima. The number of multiple equivalence ratio perturbation maxima that can propagate on the flame surface is smaller for higher forcing amplitudes and mean equivalence ratios because flame pinching and therefore the disappearance of peak equivalence ratio perturbations occur after shorter convection times. Hence, the forcing frequency needs to be higher for such events to occur as compared with lower forcing amplitudes or mean equivalence ratios, which cause the inclination of this interference pattern.

Local equivalence ratios can become close to and even larger than unity for high forcing amplitudes. Towards stoichiometric combustion, the flame speed and local enthalpy release alterations decrease for increasing equivalence ratios and the flame speed exhibits reduces beyond this limit. Since these two mechanisms govern the gain amplification caused by equivalence ratio perturbations, the gain pattern reduces beyond this point where the equivalence ratio impact saturates and the gain decays rapidly thereafter. This is even more visible in the time delay coefficient distribution. As can be seen in Fig. 8, the minimal time span until flame pinching occurs is independent of the mean equivalence ratio. However, the forcing amplitude at which it takes place changes with the mean equivalence ratio. At higher forcing amplitudes than this point, the time delay coefficient amplitudes decay rapidly.

The impact of mean velocity alterations is similar but opposite to the impact of mean equivalence ratio modifications. The mean velocity affects the flame length and thereby the propagation distance of an equivalence ratio perturbation until the flame pinches.

Further modelling The high amplification of the heat release rate oscillation at low forcing amplitudes generated due to correlated motion of the flame tip is unrealistic for a turbulent flame. Several additional modelling strategies can be employed to overcome this problem. The impact of perturbation convection in the supply duct, stochastic fluctuations at the flame and flame curvature effects are addressed here.

Applying a radially non-uniform equivalence ratio perturbation can be caused by non-equally distributed fuel injection, which reduces symmetry of the flame setup. Thereby, the coherence of the flame response at the flame tip and flame-pinching events is reduced. This causes a significant reduction of the gain, as shown in Fig. 10 (a), where a cosine distribution[†] has been employed. Figure 5 illustrates that the impact on the gain is seen especially at large forcing amplitudes.

The convention in the duct distorts the equivalence ratio perturbation profile discharging at the burner orifice. Incorporating the convection with a turbulent flow profile (Okiishi 1965) into the modelling approach[‡], the boundary layers delay the arrival of the equivalence ratio perturbations at the flame front. Therefore, the intrinsic time delay is increased, as can be seen in Fig. 10 (b). Further, the distribution of equivalence ratio perturbations leads to a flame elongation, which causes a shift of the inclined interference gain pattern towards higher forcing frequencies. The coherence of the heat release response and oscillations due to the inclined gain interference pattern are reduced, which is more evidently visible in Fig. 5. It was observed that the impact on the gain is highly dependent on the particular

[†]A cosine distributed profile between 0 and $\pi/2$ with higher magnitudes at the inner radius is initially chosen such that the inner equivalence ratio value corresponds to the equivalence ratio perturbation amplitude calculated by Eq. 11 and the outer value is the mean equivalence ratio. Further, the profile is scaled in order to conserve the mean of the equivalence ratio perturbation amplitude.

[‡]The numerical domain is extended to incorporate the entire supply duct, where the same discretisation scheme is employed as in the combustor domain to convect the equivalence ratio perturbations as passive scalar with the imposed profile.

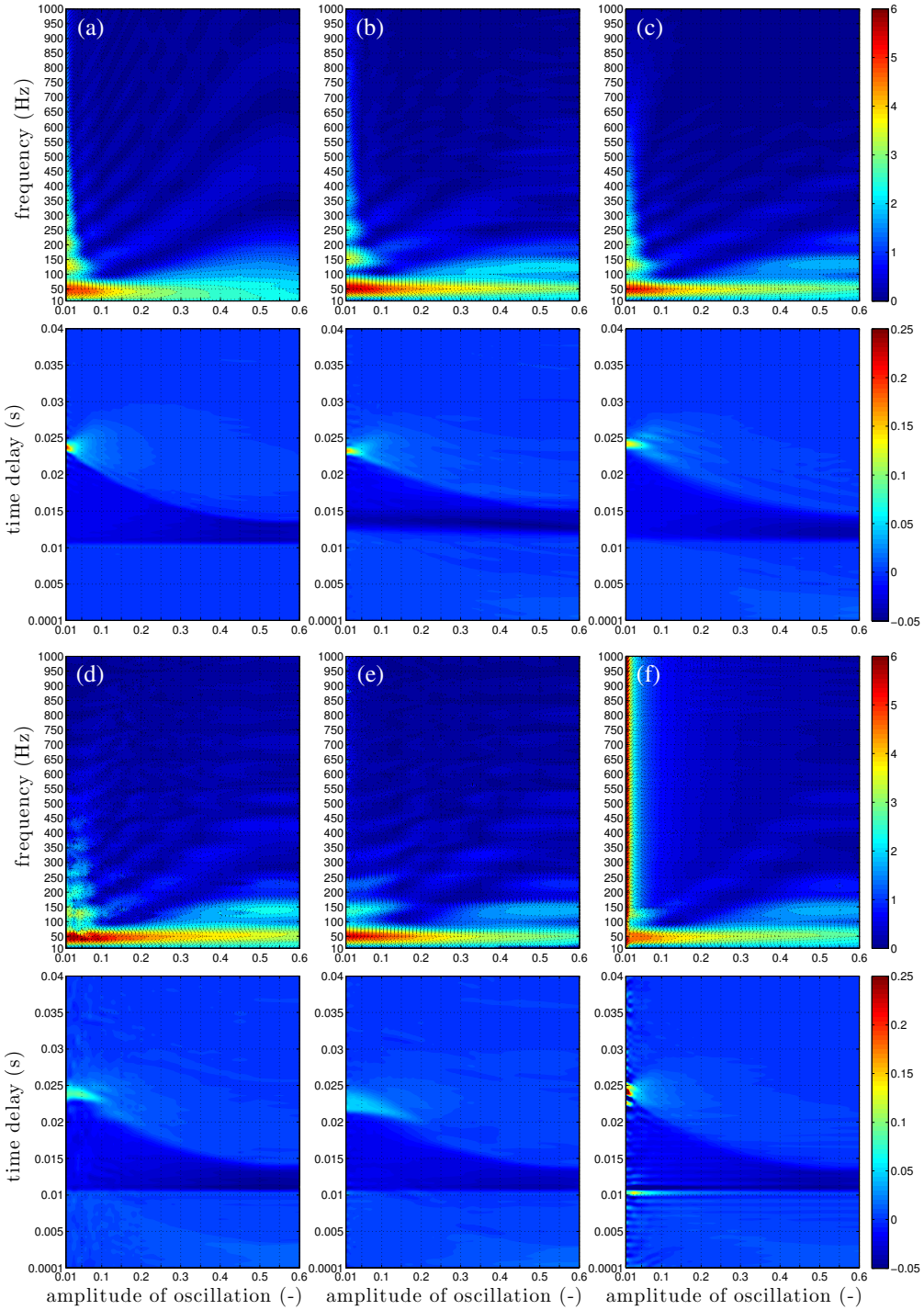

Figure 10. The effect of an asymmetric equivalence perturbation profile (a), a turbulent flow profile in the duct (b), stochastic perturbations in the supply duct (c), low (d) and high (e) frequent stochastic perturbations in the combustion chamber, and flame curvature effects (f) on the flame describing functions are illustrated for a mean equivalence ratio $\overline{\phi}$ of 0.55.

turbulent flow profile imposed. A laminar flow profile can even increase the gain.

Stochastic fluctuations (of 10% of the mean velocity) imposed on the top-hat flow in the supply duct each time step disperse the equivalence ratio perturbations. Therefore, the gain is reduced as shown in Fig. 10 (c), which can be especially noted at high forcing frequencies.

Locally high curvature of the flame front causes the flame speed to increase, which occurs especially at the flame tip and with flame-pinching events. Flame wrinkling is damped when the curvature effects are taken into account, which occurs foremost at high forcing frequencies. At very low forcing amplitudes, the heat release rate modulation is primarily generated at the flame tip (with the present velocity model). Hence, it is expected that the heat release gain is dispersed in these regions when curvature corrections are considered, which can be observed in Fig. 10 (a).

Stochastic fluctuations can be imposed frequently (altered each time step) or infrequently (imposed over several time steps) in the combustion chamber, where the fluctuation amplitude has been assumed to increase with the radial distance from the burner orifice and reach 10% of the mean

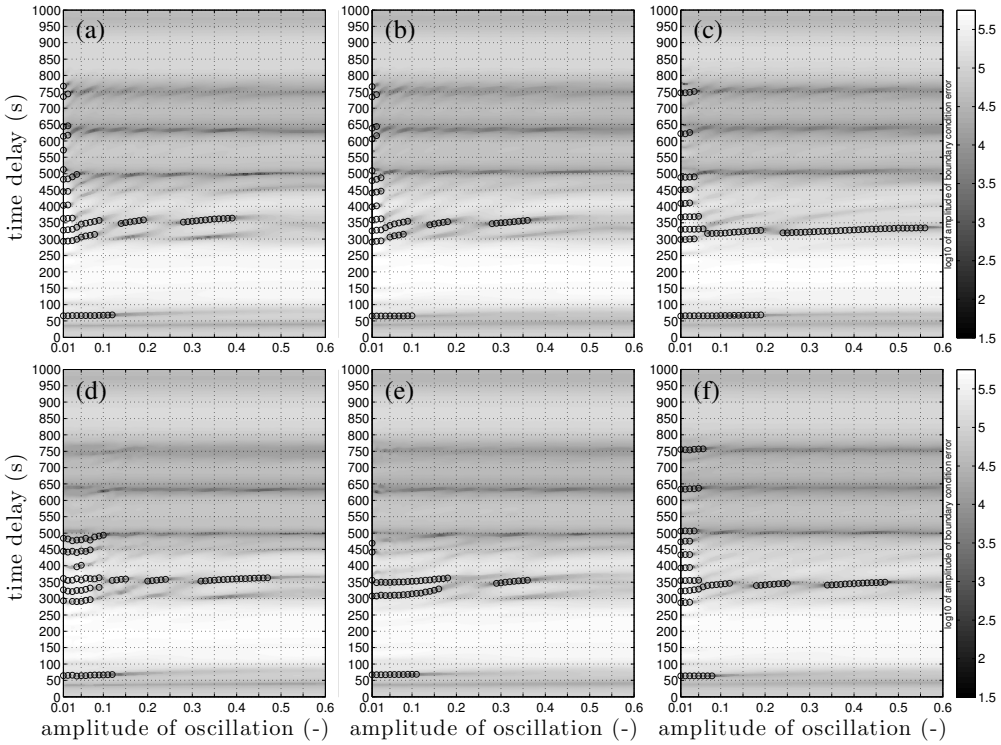

Figure 11. Logarithmic boundary condition error at the outlet as a function of frequency and nonlinear oscillation amplitude at the flame, where the equivalence ratio $\overline{\phi}$ is 0.55 and the combustor length is $350\ mm$. Modes with positive growth rate are indicated as circles. The reference case with time delay modelling is shown in (a). The impact of an equivalence ratio perturbation and turbulent flow profile is shown in (b) and (c), respectively. Flame curvature effects are considered in (d). The effect of stochastic flow fluctuations in the combustion chamber and in the supply duct is plotted in (e) and (f), respectively.

velocity at the flame tip. Frequent stochastic fluctuations disperse the gain and cause a similar gain pattern as obtained considering flame curvature effects. It is worth noting that the linear regime is extended to higher forcing amplitudes.

Infrequent stochastic fluctuations imposed in the combustion chamber additionally amplify the gain, since the velocity fluctuations are not contained in the reference velocity u_B. As shown in Fig. 10 (c), these infrequent stochastic fluctuations overlay the gain generation at frequencies beyond the first gain minima. This manifests as a high and low peak at the intrinsic time delay indicating that the addition acts as hydrodynamic source.

Limit cycle prediction

Information-rich flame describing functions have been obtained with the aim of predicting thermo-acoustic limit cycles more accurately. An acoustic network approach is used for limit-cycle prediction, which has been described in detail by Stow and Dowling (2004). Essentially, the thermo-acoustic problem is separated into propagation-like sections, which are linked by jump conditions. The heat release response of the flame represents one of these jump conditions and is modelled by the sum of time delays approach described in Eq. 2. The governing equations are decomposed into mean and perturbation contributions, while the latter are reformulated in terms of characteristic waves. These perturbations are propagated through the network, starting from known inlet conditions towards the outlet conditions. The state of the wave perturbations will not always satisfy the outlet boundary condition and therefore this perturbation exhibits a positive or negative growth rate. When the outlet boundary condition error vanishes for a wave perturbation with a non-zero amplitude and zero growth rate, a limit cycle is found. The limit cycle is stable when the growth rate decays with increased forcing amplitude and is unstable otherwise.

Many unstable thermo-acoustic modes with positive growth rates can be observed in Fig. 11 (a) at low forcing amplitudes when flame curvature effects are neglected. These arise due to the high gain estimated in the linear regime and the steep phase decay. Nonetheless, a limit cycle at a frequency of approximately $350\ Hz$ is predicted, which is in agreement with the findings by Balachandran (2005), who quotes a frequency of $348\ Hz$. However, the growth rate of this mode oscillates due to the inclined interference pattern. An unstable mode manifests at $60\ Hz$, which has a long wavelength. Accounting for the room as part of the piping network leads to a significant reduction of the growth rate for this mode.

When the equivalence ratio perturbation is non-uniform, Fig. 11 (b) shows that the estimated boundary condition error distribution is similar to that for a uniform equivalence ratio perturbation. However, the limit cycles establish at lower forcing amplitudes due to the reduced gain.

Modelling the supply duct convection with a turbulent flow profile leads to a slight frequency shift of the limit cycle to $345\ Hz$ and increases its amplitude (see Fig. 11 (c)). The reduced gain oscillations observed in Fig. 5 let the unstable mode appear nearly continuously over the forcing amplitudes.

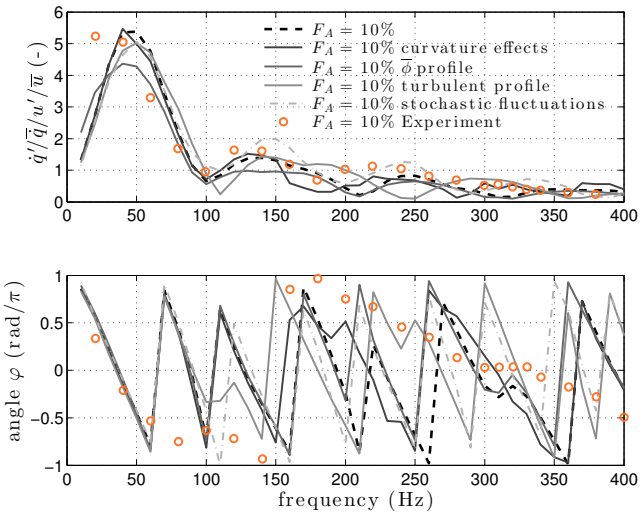

Figure 12. Quantitative comparison of the flame describing functions at a constant forcing amplitude F_A of 10%.

Considering flame curvature effects does not change the estimated limit cycle frequency (as shown in Fig. 11 (d)), but does change its amplitude. Further, fewer unstable modes are seen with low oscillation aptitudes, although they remain unstable until higher amplitudes. These differences can be explained by comparing Fig. 7 (c) and Fig. 10 (d) more thoroughly. It can be noted that the gain decays rapidly to low values at low oscillation amplitudes when flame curvature effects are not considered. In contrast, the gain is initially lower for low oscillation amplitudes but remains higher until higher amplitudes, due to flame curvature effects. Further, the inclined interference pattern shifts towards higher oscillation amplitudes accounting for flame curvature effect, which leads to the increase of the predicted limit cycle amplitude.

Frequent stochastic fluctuations, which are imposed each time step, generally reduce the gain. Figure 11 (e) shows that this reduction leads to fewer unstable modes when the stochastic fluctuations are imposed in the combustion chamber. When fluctuations are imposed in the supply duct (see Fig. 11 (f)), the distribution of modes with positive growth rates remains similar to the distribution without curvature corrections. Also, the inclined interference pattern is shifted to higher forcing amplitudes with this approach, which translates limit cycles to higher amplitudes.

Unsteady heat release oscillations can only add energy to the acoustic field when they are sufficiently in-phase with the pressure oscillations. With a steep phase decay of the flame describing function, this condition is easily met over a range of frequencies. Figure 12 shows the predicted phase behaviour of the flame describing functions considering flame curvature effects, an equivalence ratio profile, a turbulent flow profile in the supply duct, and stochastic fluctuations in the combustion chamber. It can be noted that the phase decay is less steep when a turbulent flow profile is employed to convect the equivalence ratio perturbations in the supply duct. At approximately $350\ Hz$, the differences in the phase lag are small between the modelling approaches and the dominant limit cycle is predicted at this frequency with all flame describing functions. However, the predicted limit cycle amplitudes vary significantly depending on the modelling approaches used.

Discussion

Figure 13 summarises the challenges of modelling imperfectly premixed flames with complex shapes by comparing the time delay coefficients of experimental data and two G-equation models. The time delay coefficients of the experimentally obtained data by Balachandran (2005) exhibit a narrow high-amplitude peak at small time delays. Orchini and Juniper (2015) performed G-equation simulations of the same burner geometry, where only the large-scale flow structures were modelled and the influence of equivalence ratio perturbations neglected. Figure 13 reveals that the initial high peak is similarly represented as within the experimental data, while the large negative time delay coefficients are absent. This indicates that this first peak corresponds to heat release modulation caused by large-scale flow structures, which is not present in the estimation with the present model.

Equivalence ratio perturbations, which are the focus of this study, manifest themselves as negative coefficient distribution retarded by convection in the supply duct to higher time delays. The estimated amplitudes of the negative time delay coefficients are similar to those contained in the experimental data. Nevertheless, sharp transitions from positive to negative and negative to positive time delay coefficients are predicted with the present approach, which correspond to the convection time of equivalence ratio perturbations travelling in the supply duct and the duration of equivalence ratio perturbations propagating on the flame front until the first pinching occurs, respectively. In contrast, the experimental data set exhibits a smooth transition.

Sharp time delay coefficient alterations lead to a steep phase decay, whereas smooth distributions result in a flat phase decay (Blumenthal et al. 2013). All modelling approaches estimate the phase response to be too steep. It seems therefore that this remains a significant challenge for low-order flame models.

Figure 3 shows that even the unforced flame shape is distorted by unsteady flow structures. Further, Fig. 6 reveals that the instantaneous heat release of the experimental flame exhibits cycle to cycle variations due to unsteady flow. Thus the heat release does not take place at the same location every cycle. Instead there are small-scale stochastic fluctuations and the response is dispersed. Sattelmayer (2000) stresses the importance of turbulent dispersion and the resultant impulse response distribution over time delays on limit cycle prediction. Shin and Lieuwen (2013) argue similarly and describe how stochastic flow fluctuations, on average, smooth wiggles of a premixed flame by modifying the linearised G-equation formulation. Accounting for small-scale stochastic fluctuations or flame curvature effects smooths the heat release response at the flame tip, especially at low forcing amplitudes. However, this does not improve the comparison to experimental data at a forcing amplitude of 10%.

Another modelling challenge is to deal with the artificially abrupt coefficient transition at the intrinsic time delay corresponding to the equivalence ratio perturbation propagation in the supply duct, which is between 0.01 and

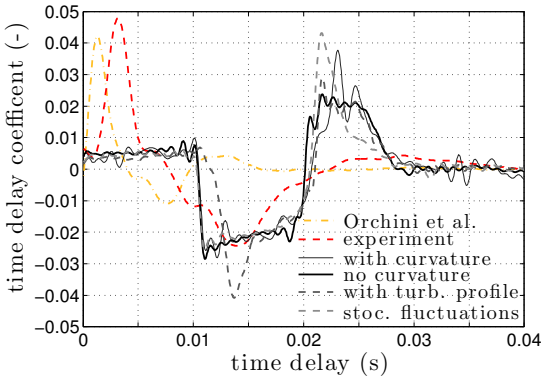

Figure 13. Comparison of time delay coefficients obtained from simulation data, experimental data by Balachandran (2005), and data by Orchini and Juniper (2015). The mean equivalence ratio $\overline{\phi}$ is 0.55 and the forcing amplitude F_A is 10%.

0.015 s in Fig. 13. With the present approach (neglecting large-scale flow structures), a smooth transition in the time delay coefficients can only be obtained by modelling the dispersion and convection of mixture fraction perturbations in the supply duct. Alternatively, the smooth transition may be caused by the large-scale flow structures and consequential flame restoration (Blumenthal et al. 2013), as suggested by the fact that the time delay coefficients found by Orchini and Juniper (2015), which included large-scale flow structures, have negative values.

For medium/large forcing amplitudes, only low equivalence ratio perturbations, which are in-phase with the velocity perturbations, propagate far enough into the combustion chamber to be affected by large-scale flow structures. In the present investigation, the velocity perturbations influence the gain by redistributing the equivalence ratio perturbations, rather than by wrinkling the flame and causing a heat release modulation directly. Analogously, the large-scale incompressible flow structures could shift this contribution of the low equivalence ratio perturbations between 0.02 and 0.03 s to earlier time delays, thereby spreading them out. To incorporate this effect, the impact of equivalence ratio and flow perturbations must be coupled.

Conclusions

Flame describing functions (FDFs) have been calculated for an axisymmetric M-flame using a level set approach. The FDFs characterise the unsteady heat release caused by imposed velocity fluctuations over a wide range of forcing frequencies and amplitudes. Velocity fluctuations of the air cause equivalence ratio perturbations because the mass flow-rate of fuel is constant, while that of the air varies. Equivalence ratio perturbations form at the fuel injector, which lies upstream of the dump plane, are convected down a duct and are then convected to the flame front by a simple analytical flow: a spherical source term with oscillating source strength. On the one hand, the FDFs are used to predict limit cycle amplitudes of thermo-acoustic oscillations. On the other hand, they are also analysed by decomposing them into a sum of time delay coefficients, which reveals the physics behind the heat release characteristics of the flame.

The numerical results have been compared with experimental data. Reasonable comparison was achieved in terms of the heat release gain at constant forcing amplitudes and instantaneous heat release rates at constant forcing frequency. This indicated that the heat release gain can be estimated neglecting large-scale flow structures and turbulence, since these phenomena contributed little to the overall gain.

However, large-scale flow structures and turbulence influence the phase decay and the gain oscillations due to the interference of equivalence ratio perturbations as they travel along the flame-front. Broadband flow fluctuations smooth out these interference patterns and disperse the heat release response over wider ranges of time delays. These smoothly-distributed time delay coefficients lead to a less steep phase decay of the heat release, which is more in line with experimental data.

In summary, the unphysically steep phase decay of the FDF in this model leads to over-prediction of the number of unstable thermo-acoustic modes, particularly at high frequencies. In addition, the inclined interference pattern (Fig. 8), but which would be smoothed out in a turbulent flame, causes the growth rates around a given frequency to oscillate around zero as the amplitude varies (e.g. in Fig. 11 around 350 Hz). Nevertheless, the predicted limit cycle frequency agrees well with experiments and the limit cycle amplitude, although quite strongly affected by the physical features of the model, is reasonably close to the experimentally observed amplitude of 0.6. This level set approach, combining mixture fraction oscillations and a simple velocity model therefore has proven to be a quick and reasonably accurate tool with which to calculate limit cycle amplitudes and frequencies of thermo-acoustic oscillations for an axisymmetric burner.

Acknowledgements

This work was conducted within the EU 7th Framework Project Joint Technology Initiatives - Clean Sky (AMEL-Advanced Methods for the Prediction of Lean-burn Combustor Unsteady Phenomena), project number: JTI-CS-2013-3-SAGE-06-009 / 641453. This work was performed using the Darwin Supercomputer of the University of Cambridge High Performance Computing Service (http://www.hpc.cam.ac.uk/), provided by Dell Inc. using Strategic Research Infrastructure Funding from the Higher Education Funding Council for England and funding from the Science and Technology Facilities Council.

References

Balachandran R (2005) *Experimental investigation of the response of turbulent premixed flames to acoustic oscillations*. PhD Thesis, University of Cambridge.

Blumenthal RS, Subramanian P, Sujith R and Polifke W (2013) Novel perspectives on the dynamics of premixed flames. *Combustion and Flame* 160(7): 1215–1224.

Dowling AP (1999) A kinematic model of a ducted flame. *Journal of fluid mechanics* 394: 51–72.

Graham OS and Dowling AP (2011) A low-order modelling of ducted flames with temporally varying equivalence ratio in realistic geometries. In: *ASME 2011 Turbo Expo: Turbine Technical Conference and Exposition*. American Society of Mechanical Engineers, pp. 277–288.

Hartmann D, Meinke M and Schröder W (2010) The constrained reinitialization equation for level set methods. *Journal of computational physics* 229(5): 1514–1535.

Huber and Polifke (2009a) Dynamics of practical premixed flames, part i: model structure and identification. *International journal of spray and combustion dynamics* 1(2): 199–228.

Huber A and Polifke W (2009b) Dynamics of practical premixed flames, part ii: identification and interpretation of cfd data. *International journal of spray and combustion dynamics* 1(2): 229–249.

Komarek T and Polifke W (2010) Impact of swirl fluctuations on the flame response of a perfectly premixed swirl burner. *Journal of Engineering for Gas Turbines and Power* 132(6): 061503.

Lieuwen T (2003) Modeling premixed combustion-acoustic wave interactions: A review. *Journal of Propulsion and Power* 19(5): 765–781.

Macquisten M, Whiteman M, Stow S and Moran A (2014) Exploitation of measured flame transfer functions for a two-phase lean fuel injector to predict thermoacoustic modes in full annular combustors. In: *ASME Turbo Expo 2014: Turbine Technical Conference and Exposition*. American Society of Mechanical Engineers, pp. V04AT04A003–V04AT04A003.

Okiishi TH (1965) *Fluid velocity profile development for turbulent flow in smooth annuli*. PhD Thesis, Iowa State University.

Orchini A and Juniper MP (2015) Heat release response to forced flow oscillations of a low-order modelled laboratory scale dump combustor. In: *ASME Turbo Expo 2015: Turbine Technical Conference and Exposition*. American Society of Mechanical Engineers, pp. V04BT04A013–V04BT04A013.

Peng D, Merriman B, Osher S, Zhao H and Kang M (1999) A pde-based fast local level set method. *Journal of Computational Physics* 155(2): 410–438.

Sattelmayer T (2000) Influence of the combustor aerodynamics on combustion instabilities from equivalence ratio fluctuations. In: *ASME Turbo Expo 2000: Power for Land, Sea, and Air*. American Society of Mechanical Engineers, pp. V002T02A003–V002T02A003.

Sethian JA (2001) Evolution, implementation, and application of level set and fast marching methods for advancing fronts. *Journal of Computational Physics* 169(2): 503–555.

Shin DH and Lieuwen T (2013) Flame wrinkle destruction processes in harmonically forced, turbulent premixed flames. *Journal of Fluid Mechanics* 721: 484–513.

Stow SR and Dowling AP (2004) Low-order modelling of thermoacoustic limit cycles. In: *ASME Turbo Expo 2004: Power for Land, Sea, and Air*. American Society of Mechanical Engineers, pp. 775–786.